

Creation of ultracold heteronuclear *p*-wave Feshbach molecules

Fan Jia,^{1,*} Zhichao Guo,^{1,†} Zerong Huang,^{1,2} and Dajun Wang^{1,2,‡}

¹*Department of Physics, The Chinese University of Hong Kong, Hong Kong, China*

²*State Key Laboratory of Quantum Information Technologies and Materials,*

The Chinese University of Hong Kong, Hong Kong SAR, China

(Dated: January 21, 2026)

We report the creation of optically trapped ultracold heteronuclear *p*-wave Feshbach molecules in a mixture of ²³Na and ⁸⁷Rb atoms. With loss spectroscopy and binding energy measurements, we systematically characterize the interspecies *p*-wave Feshbach resonances near 284 G. Leveraging this understanding, we use magneto-association to form *p*-wave NaRb Feshbach molecules, producing both pure samples and mixtures of molecules in different angular momentum states. Additionally, we investigate the inelastic loss of these molecules, primarily influenced by atom-molecule and molecule-molecule collisions. Our results represent a significant step toward realizing tunable *p*-wave interactions in heteronuclear ultracold systems and provide a foundation for exploring non-zero angular momentum molecules.

Magnetically tunable Feshbach resonances (FRs) [1] have driven significant advancements in the study of ultracold atomic gas systems by enabling precise control of inter-atomic interactions and facilitating the formation of weakly-bound Feshbach molecules (FMs) via magneto-association (MA) [2]. While *s*-wave FRs are the most commonly used, there is also substantial interest in higher partial wave FRs [3–8], which can introduce anisotropic interactions to the system [9–11] and enable investigation of exotic physics not accessible with only *s*-wave interactions [12–15].

Currently, the most studied ultracold atomic systems with higher partial wave interactions is the single-component fermions, which lack *s*-wave interactions but can exhibit tunable *p*-wave interactions near *p*-wave FRs. A range of interesting topics has been explored with such systems, including the association of *p*-wave FMs [11, 16], the *p*-wave contact [17, 18], ultracold fermions with unitary *p*-wave interactions [19], and emergent *s*-wave interactions in low dimensions [20]. Another notable study involving high partial wave interactions is the recent successful creation of a Bose-Einstein condensate (BEC) of *g*-wave Cs₂ FMs starting from a Cs atomic BEC in a two-dimensional trap [21].

Bose-Bose mixtures near *p*-wave interspecies FRs are another important system for studying physics with high partial wave interactions. As all partial waves are allowed between non-identical particles, near a *p*-wave interspecies FR, the interplay between *s*-wave interactions and the tunable *p*-wave interaction is predicted to host a range of interesting quantum phases, including superfluid with finite momentum [22, 23] and a richer miscibility phase diagram than *s*-wave only [24]. In the ⁸⁵Rb-⁸⁷Rb mixture system, several *p*-wave FRs have been observed [7, 25] and the binding energy of *p*-wave ⁸⁵Rb-⁸⁷Rb FMs was measured [25].

Besides being interesting in their own right, heteronuclear *p*-wave FMs could be transferred to the ground vibrational state via a two-photon stimulated Raman

process to form polar molecules directly in rotational levels not allowed when starting from *s*-wave FMs due to parity selection rules [26]. However, in the earlier works, samples of heteronuclear *p*-wave FMs were not obtained [7, 25]. To the best of our knowledge, creation of *p*-wave FMs has only been reported for single molecules with ²³Na and ¹³³Cs in optical tweezers [27].

In this work, we present a detailed investigation of two closely spaced *p*-wave FRs in the ²³Na and ⁸⁷Rb Bose-Bose mixture [28]. We then study the MA process and successfully created pure *p*-wave NaRb FM bulk samples in either single or mixed *m_l* states. We also observe that the pure *p*-wave NaRb FM samples can live long enough for collision studies and for transferring to the ground state. Our results provide the opportunity to unveil different loss behaviors, especially in lower dimensions [29–31], and offer a unique platform to explore novel few-body and many-body physics with high-partial wave interactions.

The two *p*-wave FRs used in this study were first observed in our previous work using ultracold thermal Na and Rb mixtures in their $|F = 1, m_F = 1\rangle$ hyperfine states, with a typical sample temperature T of about 1.8 μK [28]. Here F is the atomic hyperfine quantum number and m_F is its projection onto the quantization axis defined by the magnetic field. Based on our coupled-channel calculation [28, 32], the three resonance peaks near 284 G are assigned to the $m_f = 2$ manifold as $(m_f, m_l) = (2, -1 \& 0)$, and $(2, 1)$, with the first two peaks with $m_l = -1 \& 0$ near degenerate with each other; and the other two peaks near 285 G are assigned to the $m_f = 1$ manifold as $(1, 1)$ and $(1, 0)$. Here, m_l represents the projection of the relative rotational angular momentum or partial wave l , which, for *p*-wave scattering with $l = 1$, can be ± 1 or 0, and m_f is the projection of the total hyperfine angular momentum in the closed channel.

Here, we first characterize the *p*-wave FR with loss spectrum at different sample temperatures. Following the standard procedure detailed in [28], we prepare an

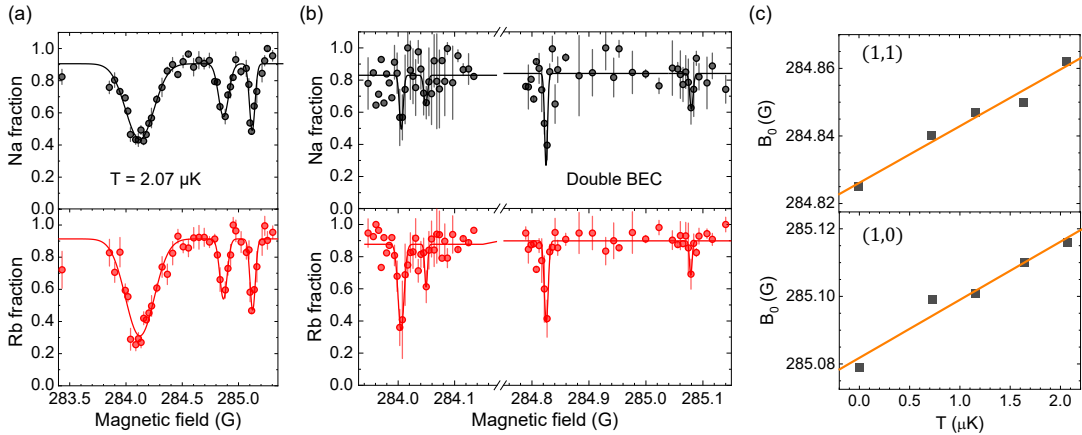


FIG. 1. Temperature dependent atom loss spectra near the 284 G *p*-wave FRs. (a) Remaining fractional Na (top) and Rb (bottom) numbers as a function of magnetic field after a 50 ms holding time for a thermal mixture at 2.07 μK . (b) The same loss measurement for a double BEC sample. For the two peaks of the $m_f = 2$ resonance (left), the holding time is 25 ms, while for the two peaks of the $m_f = 1$ resonance (right), a longer holding time of 120 ms is used. The faster losses observed for the $m_f = 2$ resonance in both (a) and (b) indicate that the coupling strength of this resonance is stronger than that of the $m_f = 1$ resonance. (c) Resonance positions B_0 as a function of sample temperature T for the $(m_f = 1, m_l = 1)$ (top) and $(1, 0)$ (bottom) peaks. The separation between the two $m_f = 2$ resonances is approximately 40 mG and they overlap at temperatures above 700 nK. The orange lines are linear fits to the slopes.

atomic mixture of Na and Rb, both in the $|1, 1\rangle$ hyperfine state, in a 1070 nm crossed optical dipole trap (ODT). The sample temperature is controlled by varying the ending trap depths of evaporative cooling. The FRs are observed by measuring the fractional loss of both Na and Rb atoms after ramping the magnetic field to a target value and holding for carefully chosen durations.

As shown in the two example measurements in Fig. 1(a) for $T = 2.07 \mu\text{K}$ and (b) for a quasi-pure double BEC, the atom loss depends strongly on temperature. The apparent narrowing of the linewidth for the double BEC compared with the thermal sample is characteristic of non-*s*-wave collisions due to the centrifugal barrier [33]. According to our coupled-channel modeling [32, 34], both FRs exhibit coupling strengths between the open and closed channels that are strong enough to categorize them as broad resonances [7, 8], with the $m_f = 2$ resonance displaying significantly stronger coupling than the $m_f = 1$ resonance, consistent with our observations. However, with the double BEC sample, our measurement shows that the resonances are still narrow in terms of magnetic field.

For the measurement taken with double BEC samples in Fig. 1(b), the four peaks, $(2, -1 \& 0)$, $(2, 1)$ for the $m_f = 2$ manifold on the left, and $(1, 1)$, $(1, 0)$ for the $m_f = 1$ manifold on the right, are fully resolved. From a double Gaussian fit to the two $m_f = 2$ peaks, we find that the separation between them is about 40 mG. We also observe that for temperatures higher than 700 nK, the two loss peaks start to merge together. At around 2 μK , they can not be resolved individually, as shown in Fig. 1(a). On the other hand, the two peaks in the

$m_f = 1$ manifold are always well separated.

Besides the varying of the loss widths, the temperature effect also causes shift of the resonance positions. The peak loss positions of the $(1, 1)$ and $(1, 0)$ peaks as a function of T are summarized in Fig. 1(c). The linear dependence on T is consistent with the theoretical results based on the trimer model [33].

To further characterize the FRs, we measure the binding energy E_b of the FMs with the magnetic field modulation method [28, 34, 35]. Near the *p*-wave resonance, a pair of Na and Rb atoms will form a FM when the magnetic field modulation frequency ν is tuned to $|E_b - E_k|/h$, where E_k is the relative kinetic energy of the atom pair. These FMs are highly prone to loss and heating from atom-molecule and molecule-molecule inelastic collisions. Consequently, the resonance can be inferred by monitoring the fractional loss of atoms or changes in the size of the remaining atomic cloud. Due to the thermal Boltzmann distribution at finite temperatures, both the linewidth and the peak position depend on temperature, and the loss and heating spectra are also asymmetric.

An example modulation association spectrum measured with loss of Na atoms for the $(1, 0)$ resonance is presented in Fig. 2(a). The temperature of the starting atomic mixture for this measurement is around 600 nK. To extract E_b , we fit the curve with a phenomenological Gaussian convoluted with a Boltzmann function. As shown in the figure, the molecular binding energy is located on the left side of the loss maximum, consistent with the intuitive expectation that additional energy is required to couple energetic atoms into molecules.

For the current system, the height of the *p*-wave barrier

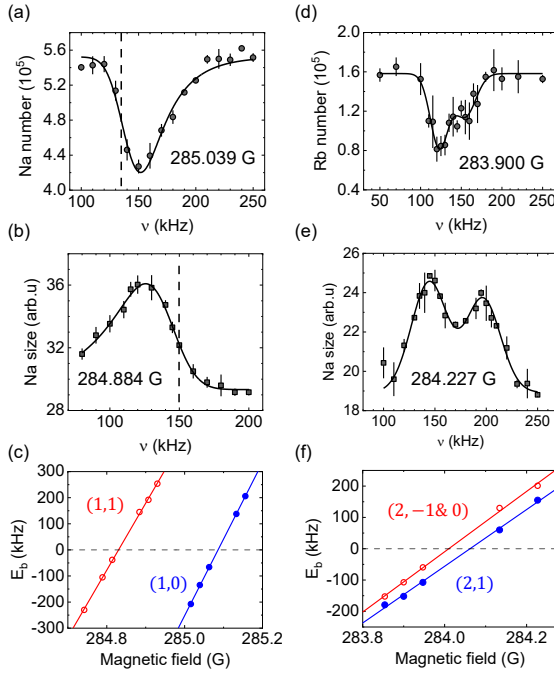


FIG. 2. Binding energy measurement by magnetic field modulation. (a) Atom loss versus the modulation frequency ν at 285.039 G for probing the (1, 0) resonance. (b) Cloud size versus ν at 284.884 G for probing the quasi-bound states associated with the (1, 1) resonance. (c) The measured binding energy E_b for (1, 1) (red circles) and (1, 0) (blue circles) resonances. (d), (e) are similar loss and heating measurements for the $m_f = 2$ manifold, respectively. The E_b difference between the two resonances is small but still resolvable. (f) shows the measured E_b for (2, -1&0) (red circles) and (2, 1) (blue circles) resonances. The solid curves in (a), (b), (d), and (e) are fits to Gaussian convoluted with Boltzmann function for extracting E_b (marked by the vertical dashed lines). The solid lines in (c) and (f) are linear fits to determine the magnetic dipole moments of the FMs relative to the atoms (the results are summarized in Table I).

is 388.7 μK [28, 34]. This is enough to support quasi-bound FMs which are subject to fast dissociative decay via tunneling. As the trap depths for both atoms are larger than the binding energy, the fragmented atoms stay in the trap and result in heating. For instance, as shown in Fig. 2(b), quasi-bound molecules of the (1, 1) resonance are associated at 284.884 G, and E_b is obtained by fitting the change in the Na cloud size. Notably, in contrast to Fig. 2(a), the fitted E_b is located on the right side of the peak, indicating that less energy is required to couple energetic atom pairs into quasi-bound molecules.

As shown in the example data in Fig. 2(d) and Fig. 2(e), similar loss and heating measurements can also be performed for the bound (283.900 G) and quasi-bound (284.227 G) states of the $m_f = 2$ manifold. As the (2, -1&0) and (2, 1) resonances are very close to each other, the E_b difference between them is also very small.

Thanks to the high resolution of the magnetic field modulation technique, the two resonances can still be clearly resolved.

The measured E_b for the $m_f = 1$ and $m_f = 2$ manifolds are summarized in Fig. 2(c) and (f). The results show that E_b varies linearly with the magnetic field, indicating a constant fraction of the closed channel in the dimer across the scanned range [36]. The slope of the linear fit, $\delta\mu_b^{exp}$, corresponds to the difference in magnetic moments between the open and closed channels. As summarized in Table I, the experimental measured $\delta\mu_b^{exp}$ agree well with the theoretical values $\delta\mu_b^{th}$ from coupled-channel calculations [33].

TABLE I. Experimentally measured $\delta\mu_b^{exp}$ and theoretically predicted $\delta\mu_b^{th}$ values associated with the $B = 284$ G p -wave resonances.

	$\delta\mu_b^{exp}$ (kHz/G)	$\delta\mu_b^{th}$ (kHz/G)
$m_f = 2, m_l = -1\&0$	980(5)	973 and 942
$m_f = 2, m_l = 1$	914(10)	906
$m_f = 1, m_l = 1$	2628(7)	2598
$m_f = 1, m_l = 0$	2887(107)	2990

To create p -wave FMs, we use MA by sweeping the magnetic field across a resonance from above. At first glance, the two well-separated peaks of the $m_f = 1$ manifold appear to be the most suitable choices for creating p -wave FMs. However, we were not able to observe any signals of FMs using this manifold, despite tuning of the MA parameters over a large range. We attribute this to the weak coupling strength between the open and closed channels for this manifold, which requires a very slow magnetic field sweep rate for efficient FM conversion [37, 38]. At the same time, severe atom-molecule inelastic collisions, which likely occur during the sweep, make it experimentally challenging to form detectable FMs with this resonance. On the other hand, the stronger coupling strength of the $m_f = 2$ manifold makes MA with this resonance more feasible, even though the splitting between the two peaks is only 40 mG.

To detect the first signature of p -wave FMs, we first ramp the magnetic field to 285.3 G, which is above both manifolds. We then sweep the magnetic field to 283.90 G, which is below both manifolds, at a constant rate for MA. Subsequently, we quench the magnetic field to 279.23 G, turn off the ODT, and apply a 160 G/cm gradient pulse for 1.5 ms to separate the FMs from the remaining atoms. The magnetic field quench increases the binding energy and the closed channel ratio which are important for preventing accidental dissociation and separating FMs from atoms. As shown in Table I, the differential magnetic momentum $\delta\mu_b$ between the open and closed channels is moderate but enough for us to separate the molecules from the remaining atoms, especially the lighter Na atoms, using the gradient pulse [39].

For detection, after the gradient pulse, we dissociate

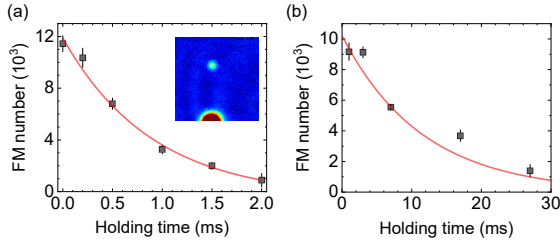


FIG. 3. First signals of *p*-wave NaRb FMs created via MA. (a) The image in the inset shows the signature of FMs (top small cloud) observed after separating them from residual atoms (bottom cloud) with a magnetic field gradient. The lifetime of the FMs in the presence of residual atoms is only 0.8(1) ms due to fast atom-molecule collisions. (b) After removal of the residual atoms, the lifetime of the pure FMs is extended to 12(3) ms. The FMs, created by sweeping the magnetic field across all resonances, are distributed among $(2, -1\&0)$ and $(2, 1)$ states. The red solid curves are exponential fits for extracting the lifetimes.

the FMs using magnetodissociation (MD) by ramping the magnetic field reversely to above the resonance and then detect the fragmented Na atoms via the high-field absorption imaging method [40]. The high-field imaging protocol involves two laser beams: an optical pumping beam that pumps the atoms to the $|2, 2\rangle$ state, and a σ^+ -polarized probe light on the cycling transition. This method can also directly probe FMs without MD, as the optical pumping beam can dissociate the FMs via photodissociation (PD). A major difference between the two dissociation methods is that PD typically results in much greater heating, especially for the lighter Na atoms. Additionally, MD can selectively dissociate FMs of different m_l states, while PD lacks such selectivity because the excited-state linewidth is much larger than the binding energies of all the FMs.

The inset of Fig. 3(a) shows the first signal of heteronuclear *p*-wave FMs obtained via MD by ramping the magnetic field to 285.3 G, which dissociates FMs of all m_l states. The FMs appear as an additional cloud above the much larger residual Na atom cloud. At an optimized MA magnetic field sweeping rate of 0.7 G/ms, up to 1.2×10^4 FMs are produced from an initial sample of 4×10^5 Na and 2×10^5 Rb atoms. This corresponds to a 6% conversion efficiency of Rb atoms into molecules, comparable to that previously achieved using the 347 G *s*-wave resonance [41].

By varying the coexistence time of the molecules and the remaining atoms in the trap at 279.23 G, we observe fast loss of FMs caused by atom-molecule collisions. As shown in Fig. 3(a), an exponential decay fit to the data yields a short FM lifetime of 0.8(1) ms.

To create a sample of FMs without residual atoms, we apply a sequence of microwave and blast light pulses after the MA process to remove the remaining Na and Rb

atoms [33]. At the end of the atom removal procedure, we typically obtain 10^4 FMs. As the magnetic field sweep crosses the whole $m_f = 2$ manifold, the FMs form as a mixture of $(2, -1\&0)$ and $(2, 1)$ states. As presented in Fig. 3(b), the lifetime of the pure FMs is 12(3) ms, much longer than that of the atom-molecule mixture.

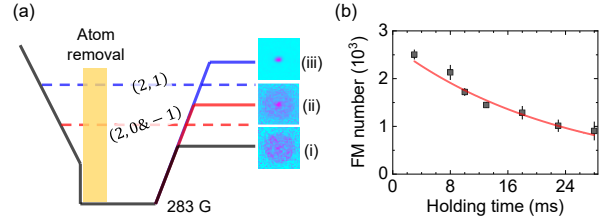


FIG. 4. Creation of pure $(2, 1)$ FMs. (a) $(2, -1\&0)$ and $(2, 1)$ FMs can be distinguished by the significantly different amount of heating of PD and MD during high-field imaging (see text for details). The red and blue dashed lines represent the positions of the $(2, -1\&0)$ and $(2, 1)$ resonances, respectively. The state of the FMs is determined by the B field endpoint of the MA process. The quench following MA is sufficiently rapid to prevent additional association. (b) The measured lifetime of the pure $(2, 1)$ FMs is 23.5(1) ms and is likely limited by excitation from the trap laser. The endpoint of the MA process is 284.056 G, which lies between the two resonances within region (ii).

The different m_l FMs can be distinguished by leveraging the distinct state selectivity and heating effects of MD and PD. As illustrated in Fig. 4(a), when the magnetic field for MD is stopped below the $(2, -1\&0)$ resonance [region (i)], all FMs are detected via PD during high-field absorption imaging. To increase the kinetic energy of the fragmented atoms from PD, the optical pumping/PD light is tuned 150 MHz above the dissociation threshold. The near 5.4 mK energy imparted to the fragmented Na atoms leads to a large and dilute cloud due to the rapid expansion during the 50 μ s time interval between PD and the probe pulse. On the other hand, when the magnetic field is ramped between the two resonances [region (ii)], the $(2, -1\&0)$ FMs are already dissociated by MD. As the heating from MD is much smaller and the fragmented atoms are not significantly heated by the imaging light pulses, this portion of the FMs appears as a more compact region in the image center. In contrast, the $(2, 1)$ FMs are dissociated by PD and appear as a much larger and more dilute region. Finally, when the magnetic field is ramped above the $(2, 1)$ resonance [region (iii)], all FMs are dissociated by MD, and only a much smaller cloud is observed. With this detection method, we also reconfirm that no $m_f = 1$ FMs are created, despite crossing the $m_f = 1$ peaks during the MA process.

The capability to distinguish different m_l states also provides a reference for creating pure $(2, 1)$ FMs. To this end, during MA, we sweep the magnetic field ending

point to region (ii). The magnetic field is then abruptly quenched to 283 G at a rate too fast to create any additional FMs. After removing the residual atoms, we obtain a pure sample of FMs at 283 G. We then ramp the magnetic field back to region (ii) for detection and to distinguish the m_l occupation of the FMs.

After fine adjustment of the MA ending point, we find that sweeping the magnetic field to 284.056 G reliably eliminates the compact center, leaving only a dilute cloud in the absorption images. This provides evidence that no $(2, -1 \& 0)$ FMs are created and that all the signals are from $(2, 1)$ FMs. After confirming this, we can then detect the pure $(2, 1)$ sample using MD by ramping the magnetic field to region (iii) for an improved SNR. Following this procedure, we can routinely produce a pure $(2, 1)$ sample containing approximately 3×10^3 FMs.

As shown in Fig. 4(b), the trap lifetime of the pure $(2, 1)$ FM sample is 23.5(1) ms. We believe that the current lifetime is affected by excitation from the trapping light, which is provided by a multi-mode laser. Previous studies of s -wave FMs have shown that the lifetime can be significantly increased by switching to a single-frequency laser [41–43]. Nevertheless, even the current lifetime is sufficient for Raman transfer to the ground state.

To summarize, we have successfully created samples of heteronuclear p -wave FMs using an ultracold mixture of Na and Rb atoms. While the current lifetime of the sample is influenced by the trapping light, future upgrades to the experimental setup will enable the study of dynamics dominated by two-body FM collisions. These advancements may also allow us to explore theoretical predictions that, in lower dimensions, the inelastic collision rate of p -wave FMs may be significantly reduced [31], paving the way for the realization of long-lived p -wave FMs.

The PD of p -wave FMs potentially allows for the study of correlations between the resulting Na and Rb atoms, such as their momentum and angular distributions, which reflect the non-zero angular momentum of the FMs [11]. However, the current detection is perpendicular to the quantization axis, which limits the resolution of angular momentum features and correlations. Future improvements, such as coincidence detection and probing along the quantization axis, could enable more detailed studies of dissociation dynamics and even entanglement between the fragments [44].

We are grateful to Bin Zhu, Yue Cui, Zhendong Zhang, and Shizhong Zhang for valuable discussions, as well as Xinyuan Gao and Yangqian Yan for their careful reading of our manuscript. This work is supported by Quantum Science and Technology–National Science and Technology Major Project of China (2024ZD0300600), the Hong Kong RGC General Research Fund (Grants 14304323 and 14302722) and the Collaborative Research Fund (Grant No. C4050-23G), and Guangdong Provincial Quantum Science Strategic Initiative (Grant No. GDZX2303002).

- [1] C. Chin, R. Grimm, P. Julienne, and E. Tiesinga, Feshbach resonances in ultracold gases, *Rev. Mod. Phys.* **82**, 1225 (2010).
- [2] T. Köhler, K. Góral, and P. S. Julienne, Production of cold molecules via magnetically tunable Feshbach resonances, *Rev. Mod. Phys.* **78**, 1311 (2006).
- [3] C. A. Regal, C. Ticknor, J. L. Bohn, and D. S. Jin, Tuning p -wave interactions in an ultracold fermi gas of atoms, *Phys. Rev. Lett.* **90**, 053201 (2003).
- [4] C. Ticknor, C. A. Regal, D. S. Jin, and J. L. Bohn, Multiplet structure of Feshbach resonances in nonzero partial waves, *Phys. Rev. A* **69**, 042712 (2004).
- [5] J. Zhang, E. G. M. van Kempen, T. Bourdel, L. Khaykovich, J. Cubizolles, F. Chevy, M. Teichmann, L. Tarruell, S. J. J. M. F. Kokkelmans, and C. Salomon, p -wave Feshbach resonances of ultracold ^6Li , *Phys. Rev. A* **70**, 030702 (2004).
- [6] K. Günter, T. Stöferle, H. Moritz, M. Köhl, and T. Esslinger, p -wave interactions in low-dimensional fermionic gases, *Phys. Rev. Lett.* **95**, 230401 (2005).
- [7] S. Dong, Y. Cui, C. Shen, Y. Wu, M. K. Tey, L. You, and B. Gao, Observation of broad p -wave Feshbach resonances in ultracold ^{85}Rb – ^{87}Rb mixtures, *Phys. Rev. A* **94**, 062702 (2016).
- [8] Y. Cui, C. Shen, M. Deng, S. Dong, C. Chen, R. Lü, B. Gao, M. K. Tey, and L. You, Observation of broad d -wave Feshbach resonances with a triplet structure, *Phys. Rev. Lett.* **119**, 203402 (2017).
- [9] A. S. Mellish, N. Kjærgaard, P. S. Julienne, and A. C. Wilson, Quantum scattering of distinguishable bosons using an ultracold-atom collider, *Phys. Rev. A* **75**, 020701 (2007).
- [10] A. C. J. Wade, D. Baillie, and P. B. Blakie, Direct simulation monte carlo method for cold-atom dynamics: Classical Boltzmann equation in the quantum collision regime, *Phys. Rev. A* **84**, 023612 (2011).
- [11] J. P. Gaebler, J. T. Stewart, J. L. Bohn, and D. S. Jin, p -wave Feshbach molecules, *Phys. Rev. Lett.* **98**, 200403 (2007).
- [12] V. Gurarie, L. Radzihovsky, and A. V. Andreev, Quantum phase transitions across a p -wave Feshbach resonance, *Phys. Rev. Lett.* **94**, 230403 (2005).
- [13] C.-H. Cheng and S.-K. Yip, Anisotropic fermi superfluid via p -wave Feshbach resonance, *Phys. Rev. Lett.* **95**, 070404 (2005).
- [14] J. Levinsen, N. R. Cooper, and V. Gurarie, Strongly resonant p -wave superfluids, *Phys. Rev. Lett.* **99**, 210402 (2007).
- [15] C. C. Tsuei and J. R. Kirtley, Phase-sensitive evidence for d -wave pairing symmetry in electron-doped cuprate superconductors, *Phys. Rev. Lett.* **85**, 182 (2000).
- [16] Y. Inada, M. Horikoshi, S. Nakajima, M. Kuwata-Gonokami, M. Ueda, and T. Mukaiyama, Collisional properties of p -wave Feshbach molecules, *Phys. Rev. Lett.* **101**, 100401 (2008).
- [17] Z. Yu, J. H. Thywissen, and S. Zhang, Universal relations for a fermi gas close to a p -wave interaction resonance, *Phys. Rev. Lett.* **115**, 135304 (2015).
- [18] C. Luciuk, S. Trotzky, S. Smale, Z. Yu, S. Zhang, and J. H. Thywissen, Evidence for universal relations describing a gas with p -wave interactions, *Nature Phys.* **12**, 599

(2016).

[19] V. Venu, P. Xu, M. Mamaev, F. Corapi, T. Bilitewski, J. P. D’Incao, C. J. Fujiwara, A. M. Rey, and J. H. Thywissen, Unitary *p*-wave interactions between fermions in an optical lattice, *Nature* **613**, 262 (2023).

[20] K. G. Jackson, C. J. Dale, J. Maki, K. G. S. Xie, B. A. Olsen, D. J. M. Ahmed-Braun, S. Zhang, and J. H. Thywissen, Emergent *s*-wave interactions between identical fermions in quasi-one-dimensional geometries, *Phys. Rev. X* **13**, 021013 (2023).

[21] Z. Zhang, L. Chen, K. X. Yao, and C. Chin, Transition from an atomic to a molecular Bose–Einstein condensate, *Nature* **592**, 708 (2021).

[22] L. Radzhivsky and S. Choi, *p*-wave resonant bose gas: A finite-momentum spinor superfluid, *Phys. Rev. Lett.* **103**, 095302 (2009).

[23] S. Choi and L. Radzhivsky, Finite-momentum superfluidity and phase transitions in a *p*-wave resonant bose gas, *Phys. Rev. A* **84**, 043612 (2011).

[24] M. Deng, M. Xue, J. Pang, H. Luo, Z. Wang, J. Li, and D. Yang, Miscibility of binary bose-einstein condensates with *p*-wave interaction, *Phys. Rev. A* **109**, 043324 (2024).

[25] S. B. Papp, *Experiments with a two-species Bose-Einstein condensate utilizing widely tunable interparticle interactions*, Ph.D. thesis, University of Colorado, Boulder (2007).

[26] T. Langen, G. Valtolina, D. Wang, and J. Ye, Quantum state manipulation and cooling of ultracold molecules, *Nat. Phys.* **20**, 702 (2024).

[27] J. T. Zhang, Y. Yu, W. B. Cairncross, K. Wang, L. R. B. Picard, J. D. Hood, Y.-W. Lin, J. M. Hutson, and K.-K. Ni, Forming a single molecule by magnetoassociation in an optical tweezer, *Phys. Rev. Lett.* **124**, 253401 (2020).

[28] F. Wang, D. Xiong, X. Li, D. Wang, and E. Tiemann, Observation of Feshbach resonances between ultracold Na and Rb atoms, *Phys. Rev. A* **87**, 050702 (2013).

[29] L. Pricoupenko, Resonant scattering of ultracold atoms in low dimensions, *Phys. Rev. Lett.* **100**, 170404 (2008).

[30] S.-G. Peng, S. Tan, and K. Jiang, Manipulation of *p*-wave scattering of cold atoms in low dimensions using the magnetic field vector, *Phys. Rev. Lett.* **112**, 250401 (2014).

[31] L. Zhou and X. Cui, Stretching *p*-wave molecules by transverse confinements, *Phys. Rev. A* **96**, 030701 (2017).

[32] J. M. Hutson and C. R. Le Sueur, molscat: A program for non-reactive quantum scattering calculations on atomic and molecular collisions, *Comput. Phys. Commun.* **241**, 9 (2019).

[33] See supplementary material.

[34] Z. Guo, F. Jia, B. Zhu, L. Li, J. M. Hutson, and D. Wang, Improved characterization of Feshbach resonances and interaction potentials between ^{23}Na and ^{87}Rb atoms, *Phys. Rev. A* **105**, 023313 (2022).

[35] S. T. Thompson, E. Hodby, and C. E. Wieman, Ultracold molecule production via a resonant oscillating magnetic field, *Phys. Rev. Lett.* **95**, 190404 (2005).

[36] J. Fuchs, C. Ticknor, P. Dyke, G. Veeravalli, E. Kuhnle, W. Rowlands, P. Hannaford, and C. J. Vale, Binding energies of ^6Li *p*-wave Feshbach molecules, *Phys. Rev. A* **77**, 053616 (2008).

[37] E. Hodby, S. T. Thompson, C. A. Regal, M. Greiner, A. C. Wilson, D. S. Jin, E. A. Cornell, and C. E. Wieman, Production efficiency of ultracold Feshbach molecules in bosonic and fermionic systems, *Phys. Rev. Lett.* **94**, 120402 (2005).

[38] T. D. Cumby, R. A. Shewmon, M.-G. Hu, J. D. Perreault, and D. S. Jin, Feshbach molecule formation in a Bose-Fermi mixture, *Phys. Rev. A* **87**, 012703 (2013).

[39] J. Herbig, T. Kraemer, M. Mark, T. Weber, C. Chin, H.-C. Nägerl, and R. Grimm, Preparation of a pure molecular quantum gas, *Science* **301**, 1510 (2003).

[40] F. Jia, Z. Guo, L. Li, and D. Wang, Detection of NaRb Feshbach molecules by photodissociation, *Phys. Rev. A* **102**, 043327 (2020).

[41] F. Wang, X. He, X. Li, B. Zhu, J. Chen, and D. Wang, Formation of ultracold narb Feshbach molecules, *New J. Phys.* **17**, 035003 (2015).

[42] F. Wang, X. Ye, M. Guo, D. Blume, and D. Wang, Observation of resonant scattering between ultracold heteronuclear Feshbach molecules, *Phys. Rev. A* **100**, 042706 (2019).

[43] M. Guo, B. Zhu, B. Lu, X. Ye, F. Wang, R. Vexiau, N. Bouloufa-Maafa, G. Quéméner, O. Dulieu, and D. Wang, Creation of an ultracold gas of ground-state dipolar ^{23}Na - ^{87}Rb molecules, *Phys. Rev. Lett.* **116**, 205303 (2016).

[44] M. Greiner, C. A. Regal, J. T. Stewart, and D. S. Jin, Probing pair-correlated fermionic atoms through correlations in atom shot noise, *Phys. Rev. Lett.* **94**, 110401 (2005).

[45] T. Maier, H. Kadau, M. Schmitt, M. Wenzel, I. Ferrier-Barbut, T. Pfau, A. Frisch, S. Baier, K. Aikawa, L. Chomaz, M. J. Mark, F. Ferlaino, C. Makrides, E. Tiesinga, A. Petrov, and S. Kotochigova, Emergence of chaotic scattering in ultracold er and dy, *Phys. Rev. X* **5**, 041029 (2015).

[46] A. Green, H. Li, J. H. See Toh, X. Tang, K. C. McCormick, M. Li, E. Tiesinga, S. Kotochigova, and S. Gupta, Feshbach resonances in *p*-wave three-body recombination within fermi-fermi mixtures of open-shell ^6Li and closed-shell ^{173}Yb atoms, *Phys. Rev. X* **10**, 031037 (2020).

[47] Z. Guo, F. Jia, L. Li, Y. Ma, J. M. Hutson, X. Cui, and D. Wang, Lee-Huang-Yang effects in the ultracold mixture of ^{23}Na and ^{87}Rb with attractive interspecies interactions, *Phys. Rev. Res.* **3**, 033247 (2021)

SUPPLEMENTAL MATERIAL

SECTION S1: TEMPERATURE-DEPENDENT ATOM-LOSS SPECTRA

A coupled-channel “trimer” model was proposed to account for the temperature-dependent three-body recombination resonance [45]. In this model, atoms from the scattering asymptote in the entrance channel can temporarily form trimers in closed channels. These trimers can subsequently break up into a weakly bound dimer and an atom in one of the open channels, followed by energy release and atom loss. The recombination rate coefficient at collision energy E_3 for this process is given

by:

$$L_3(E_3, B) = (2\lambda + 1) \frac{192\pi^2 \hbar k_3}{k_3^5 \mu_3} |S(E_3, B)|^2, \quad (\text{S1})$$

where k_3 is the relative wave vector, $\mu_3 = \sqrt{m_1 m_2 m_3 / (m_1 + m_2 + m_3)}$ is the three-body reduced mass, and λ represents the relative angular momentum. The S -matrix element $|S(E_3, B)|^2$ can be expressed as:

$$|S(E_3, B)|^2 = \frac{\Gamma(E_3)\Gamma_{\text{br}}}{[E_3 - \mu(B - B_0)]^2 + [\Gamma_{\text{tot}}(E_3)/2]^2}, \quad (\text{S2})$$

where B_0 is the trimer resonance location and μ is the relative magnetic moment between the trimer and the entrance channel. $\Gamma_{\text{tot}}(E_3)$ is the total energy width, which is the sum of the entrance-channel energy width $\Gamma(E_3) = A_\lambda E_3^{\lambda+2}$ and the decay rate of the resonance into the dimer and atom, Γ_{br} .

This trimer model effectively explains the experimentally observed temperature-dependent s - and d -wave [45], as well as p -wave [46] atom-loss spectra. The maximum loss rate coefficient of the s - and d -wave Feshbach resonances (FRs) both vary with temperature, albeit in opposite manners [45]. In contrast, for the p -wave resonance, the maximum loss rate coefficient is independent of temperature under the condition $k_B T \gg \Gamma_{\text{br}} \gg \Gamma(E)$ [46]. In our experiment, we did not observe a clear temperature dependence of the loss maxima for all resonances when the temperature exceeded 700 nK. However, while scanning the $m_f = 1$ resonances in the case of a dual Bose-Einstein condensate (dBEC), we needed to extend the holding time from the typical 50 ms to 120 ms to achieve the same loss ratio. This suggests a reduced maximum atom-loss rate coefficient in the quantum degeneracy regime.

Under the condition $k_B T \gg \Gamma_{\text{br}} \gg \Gamma(E)$, the Lorentzian function in Eq. (S2) can be approximated as a delta function peaked at $E = \mu(B - B_0)$. Substituting this into Eq. (S1) and averaging the three-particle recombination rate $L_3(E, B)$ with a Maxwell-Boltzmann distribution over the relative three-body collision energy E , the position of maximum atom loss correlated with temperature follows:

$$B = B_0 + (2 + \lambda) \frac{k_B T}{\mu}, \quad (\text{S3})$$

where $\lambda = 1$ for the p -wave FRs. From the fitted slopes, we obtain the relative magnetic moment between bound trimers and entrance channels: $\mu = 3732$ kHz/G for the $(1, 1)$ resonance and $\mu = 3636$ kHz/G for the $(1, 0)$ resonance. We also note that, similar to Ref. [46], these slopes lie between $\delta\mu_b$ and $2\delta\mu_b$ (as shown in Table 1 of the main text). This possibly indicates that the bound trimer can be regarded as a superposition state of one $^{23}\text{Na}^{87}\text{Rb}$ pair in the dimer resonant state and two $^{23}\text{Na}^{87}\text{Rb}$ dimers in the resonant state.

From low-temperature scattering theory, for a pure BEC sample with temperature close to zero, it is predicted that no atom loss should be observed as the scattering cross-section vanishes. However, due to trap-induced confinement, atoms possess non-zero relative momentum, which explains why narrow but significant loss features are still observed.

SECTION S2: CALCULATION OF $\delta\mu_b^{\text{th}}$

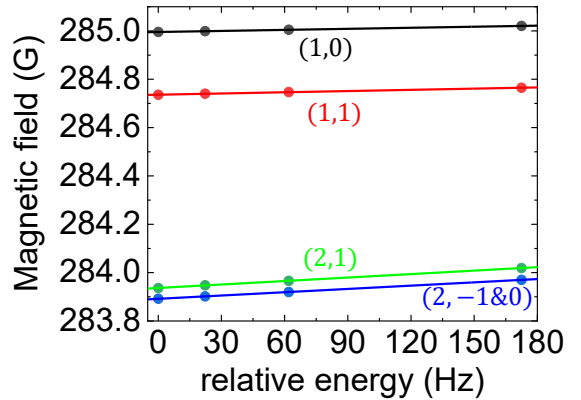


FIG. S1. Calculated resonances as a function of relative kinetic energies between two atoms. The solid lines are linear fits, and the slopes are used to derive the inverse of the magnetic moment difference $\delta\mu_b^{\text{th}}$ between the open and closed channels. The resulting $\delta\mu_b^{\text{th}}$ values are summarized in Table 1 of the main text.

Theoretical molecular binding energies were calculated using the MOLSCAT package [32], with model parameters adapted from a newly calibrated molecular potential [34]. By varying the relative kinetic energy between atoms in the open channel, we simulated the scattering cross-section as a function of the magnetic field to determine resonance locations. The calculated results for $m_f = 1$ and $m_f = 2$ resonances are summarized in Fig. S1. Linear functions are used to fit the correlation between resonance shifts and relative kinetic energies, allowing for the extraction of the theoretical magnetic moment difference $\delta\mu_b^{\text{th}}$ between the open and closed channels.

SECTION S3: FAST MAGNETIC FIELD CONTROL FOR CREATING MOLECULES

The primary magnetic field is provided by a pair of large coils. Due to limited feedback control bandwidth and Eddy current, the field typically needs over 10 ms to stabilize within 10 mG following a ramp. This residual fluctuation affects both the MA, especially in creating the pure $(2, 2)$ FMs because of the small separation between

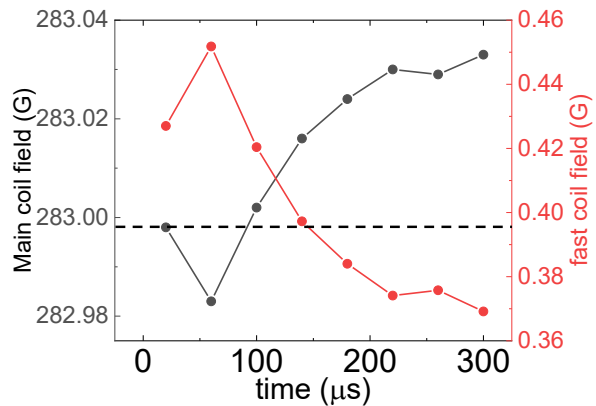


FIG. S2. Magnetic field control for fast atom removal. (Black) Magnetic field after the end of the main coil sweep. (Red) Magnetic field setting applied to the fast coil. (Dashed line) Net magnetic field after feed-forward compensation.

the peaks, and the effective state transfer of the residual atoms to the $|2, 2\rangle$ state for their rapid removal, which is necessary to increase the lifetime of the FMs. To mitigate this issue, we implemented a pair of fast-switching coils [47] and use it to actively compensate the magnetic field fluctuations using feed-forward control. An example of the magnetic field feed-forward control sequence is shown in Fig. S2. This technique has allowed for the complete removal of residual atoms using microwave and blast pulses within 300 μ s after the main coil sweep.